

Supplemental Material to “Chiral singlet superconductivity in the weakly correlated metal LaPt₃P”

P. K. Biswas,^{1,*} S. K. Ghosh,^{2,†} J. Z. Zhao,³ D. A. Mayoh,⁴ N. D. Zhigadlo,^{5,6}
Xiaofeng Xu,⁷ C. Baines,⁸ A. D. Hillier,¹ G. Balakrishnan,⁴ and M. R. Lees⁴

¹*ISIS Pulsed Neutron and Muon Source, STFC Rutherford Appleton Laboratory,
Harwell Campus, Didcot, Oxfordshire OX11 0QX, United Kingdom*

²*School of Physical Sciences, University of Kent, Canterbury CT2 7NH, United Kingdom*

³*Co-Innovation Center for New Energetic Materials,*

Southwest University of Science and Technology, Mianyang, 621010, China

⁴*Physics Department, University of Warwick, Coventry, CV4 7AL, United Kingdom*

⁵*Laboratory for Solid State Physics, ETH Zurich, 8093 Zurich, Switzerland*

⁶*CrystMat Company, 8037 Zurich, Switzerland*

⁷*Department of Applied Physics, Zhejiang University of Technology, Hangzhou 310023, China*

⁸*Laboratory for Muon Spin Spectroscopy, Paul Scherrer Institute, CH-5232 Villigen PSI, Switzerland*

(Dated: December 10, 2020)

In this Supplemental Material, we present details of the synthesis, characterization measurements, experimental methods and data analysis of the LaPt₃P samples grown at Warwick, United Kingdom and at ETH, Switzerland. We also give additional band structure results, details of the symmetry analysis and topological properties of the chiral *d*-wave state of LaPt₃P.

I. SYNTHESIS AND CHARACTERIZATION OF THE SAMPLE GROWN AT WARWICK, UNITED KINGDOM

Polycrystalline LaPt₃P [1] samples (sample-A) were synthesized by a solid state reaction method. Powders of elemental platinum, red phosphorus, and alkaline earth (lanthanum) were mixed in an argon-filled glove box, and sealed in a quartz tube filled with argon gas. The tube was initially heated to 400 °C and held at this temperature for 12 h in order to avoid rapid volatilization of phosphorus, then reacted at 900 °C for 72 h. The sintered pellet was reground and further annealed at 900 °C within argon-filled quartz tubes for several days and finally quenched into iced water.

The room-temperature structure was determined via powder x-ray diffraction (PXRD). PXRD was measured using a Bruker D5000 general purposed powder diffractometer. The diffraction pattern is shown in Fig. 1. Reitveld refinement was carried out using the TOPAS software package [2] which gave the parameters shown in Table I.

TABLE I. Crystallographic and Rietveld refinement parameters obtained on LaPt₃P.

Space-group	<i>P4nmm</i> (No. 129)			
Formula units/unit cell (Z)	2			
Lattice parameter				
<i>a</i> (Å)	5.7683(6) (at 300K)	Atom	Wyckoff Position	Occupancy
<i>c</i> (Å)	5.4681(7) (at 300K)	Pt(1)	4e	1
<i>V</i> _{cell} (Å ³)	182.4	Pt(2)	2c	1
		La(1)	2a	1
		P(1)	2c	1
				x
				y
				z
				0.25 0.25 0.5
				0 0.5 0.1476(8)
				0 0.5 0.758(4)
				0 0 0

The heat capacity in zero field was measured using a Quantum Design Physical Property Measurement System (PPMS) with a He³ insert to get down to 0.5 K. The total specific heat C_{tot} at low temperatures is made up of several contributions,

$$C_{tot} = C_{el} + C_{ph} + C_{hyp} \quad (1)$$

where C_{el} is the electronic specific heat having the form in the normal state

$$C_{el} = \gamma_n T \quad (2)$$

with γ_n being the Sommerfeld coefficient, C_{ph} is the specific heat due to the phonons given by

$$C_{ph} = \beta_3 T^3 + \beta_5 T^5 \quad (3)$$

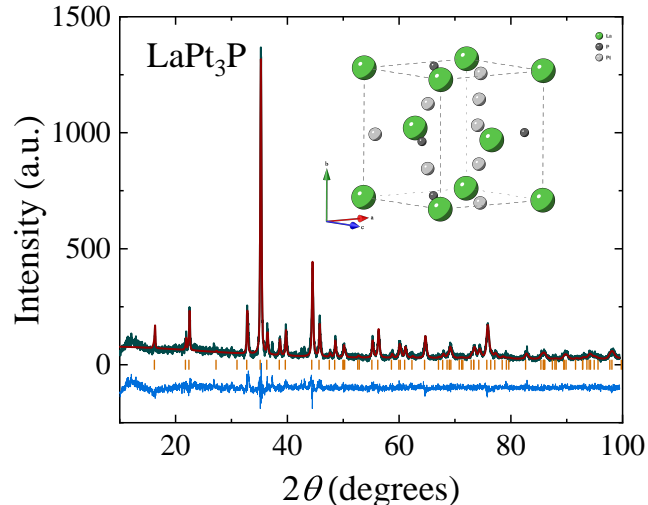


FIG. 1. **Powder x-ray diffraction pattern of the sample-A of LaPt_3P at room temperature.** X-ray diffraction pattern of LaPt_3P at room temperature where the green, red and blue lines indicate the experimental data, the fit and the difference between the data and the fit, respectively. The orange dashes indicate the expected Bragg peaks. The inset shows the structure of a unit cell of LaPt_3P .

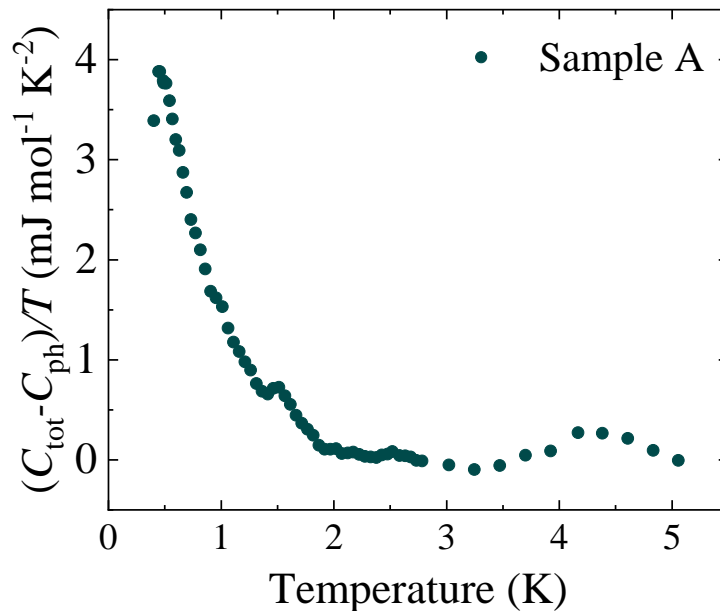


FIG. 2. **Heat capacity of the sample-A of LaPt_3P in zero-field.** $(C_{\text{tot}} - C_{\text{ph}})/T$ as a function of temperature. There is a small anomaly close to the expected superconducting transition temperature that is masked by a large hyperfine contribution.

with β_3 and β_5 being temperature independent parameters, and C_{hyp} is a contribution due to hyperfine splitting

$$C_{\text{hyp}} \propto 1/T^2. \quad (4)$$

Fitting the normal state specific heat gives $\gamma_n = 9.78(7)$ mJ/mol-K, $\beta_3 = 0.369(14)$ mJ/mol-K⁴ and $\beta_5 = 5.47(5)$ $\mu\text{J}/\text{mol-K}^4$. We then subtract the phonon contribution to the specific heat to plot the electronic specific heat including the hyperfine contribution. This is shown in the Fig. 2 for the sample-A of LaPt_3P , and is consistent with the previous measurement of Ref.[1]. We note that the specific heat has a small anomaly close to the expected $T_c \approx 1.1$ K which is obscured by an upturn at lower temperatures. This is due to a large hyperfine contribution to the specific heat.

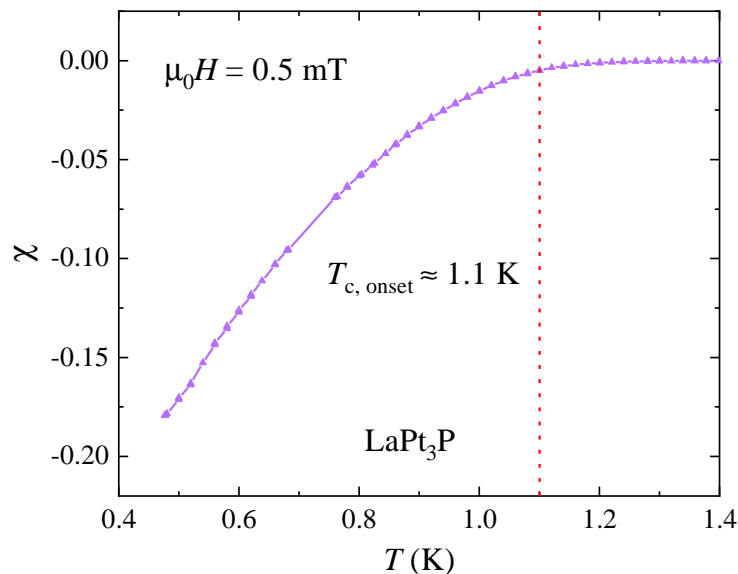


FIG. 3. Zero-field-cooled magnetic susceptibility of the sample-A of LaPt_3P as a function of temperature.

The magnetic susceptibility was measured using a Quantum Design Magnetic Property Measurement System (MPMS) using an i-quantum ^3He insert. As seen from Fig. 3 this sample has a relatively low Meissner fraction ($\sim 30\%$).

II. SYNTHESIS AND CHARACTERIZATION OF THE SAMPLE GROWN AT ETH, SWITZERLAND

A polycrystalline sample of LaPt_3P (sample-B) was synthesized using the cubic anvil high-pressure and high-temperature technique. Starting powders of LaP and Pt of high purity (99.99%) were weighed according to the stoichiometric ratio, thoroughly ground, and enclosed in a boron nitride container, which was placed inside a pyrophyllite cube with a graphite heater. The details of experimental setup can be found in Ref.[3]. All the work related to the sample preparation and the packing of the high pressure cell-assembly was performed in an argon-filled glove box. In a typical run, a pressure of 2 GPa was applied at room temperature. The temperature was ramped in 3 h to the maximum value of 1500 °C, maintained for 5 h, and then cooled to 1350 °C over 5 h and finally reduced to room temperature in 3 h. Afterward, the pressure was released, and the sample was removed. The sample exhibits a large diamagnetic response with the superconducting transition temperature of 1.1 K.

Susceptibility measurements were performed using a Quantum Design Magnetic Property Measurement System (MPMS) by cooling the sample at base temperature in zero field and then apply 7 mT magnetic field. Data were collected while warming up the sample temperature. As shown in the main text, the temperature dependence of the susceptibility data shows a bulk superconducting transition with a T_c at around 1.1 K.

A virgin magnetisation curve was measured at 0.63 K in a Quantum Design MPMS. A linear deviation of the magnetisation curve at low field region (see Fig. 4) shows that the lower critical field H_{c1} of LaPt_3P is around 1 mT.

III. μSR TECHNIQUE

μSR is a very sensitive local magnetic probe utilizing fully spin-polarized muons [4]. In a μSR experiment polarized muons are implanted into the host sample. After thermalization, each implanted muon decays (lifetime $\tau_\mu = 2.2 \mu\text{s}$) into a positron (and two neutrinos) emitted preferentially in the direction of the muon's spin at the time of decay. Using detectors appropriately positioned around the sample, the decay positrons are detected and time stamped. From the collected histograms, the asymmetry in the positron emission as a function of time, $A(t)$, can be determined, which is directly proportional to the time evolution of the muon spin polarization.

μSR measurements were performed on sample-A in the MUSR spectrometer at the ISIS Pulsed Neutron and Muon Source, UK, and on sample-B in the LTF spectrometer at the Paul Scherrer Institut (PSI), Switzerland. The polycrystalline samples of LaPt_3P in the form of powder were mounted on high purity silver sample holders. The

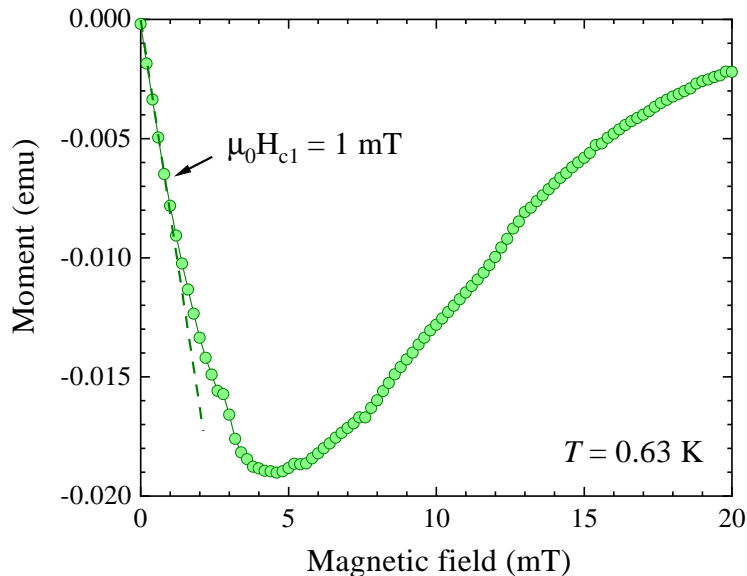


FIG. 4. **Magnetic field dependence of the virgin magnetisation curve for sample-B of LaPt₃P.** We note that the lower critical field $\mu_0 H_{c1} \approx 1$ mT.

samples were cooled from above T_c to base temperature in zero field for ZF- μ SR measurements, and in a field for the TF- μ SR measurements. The external field was 10 mT for the TF- μ SR measurements performed at ISIS and was 7 mT for the TF- μ SR measurements performed at PSI. ZF- μ SR measurements were performed in true zero field, achieved by three sets of orthogonal coils working as an active compensation system which cancel any stray fields at the sample position down to $1.0 \mu\text{T}$. LF- μ SR measurements were also performed under similar field-cooled conditions. The typical counting statistics were ~ 40 and ~ 24 million muon decays per data point at ISIS and PSI, respectively. The ZF-, LF- and TF- μ SR data were analyzed using the equations given in the text.

The zero temperature upper critical field for LaPt₃P, $\mu_0 H_{c2} \approx 0.12$ T which is much larger than the applied transverse fields in the TF- μ SR measurements. The detailed parameters for the analysis of superfluid density data from the TF- μ SR measurements for the two samples using the different gap models mentioned in the main text are given in the Table II.

TABLE II. Summary of the analysis of the superfluid density data for the two samples of LaPt₃P.

Model	$g(\theta, \phi)$	Gap type	Reduced least-squared deviation (χ_r^2)	Fitted $\Delta_m(0)/(k_B T_c)$
<i>s</i> -wave	1	nodeless	13.025	1.270 ± 0.020
<i>p</i> -wave	$\sin(\theta)e^{i\phi}$	two point nodes	4.537	1.693 ± 0.029
chiral <i>d</i> -wave	$\sin(2\theta)e^{i\phi}$	two point nodes + a line node	2.238	1.989 ± 0.011

IV. BAND STRUCTURE

LaPt₃P crystallizes in a centrosymmetric primitive tetragonal crystal structure. The corresponding space group is P4/nmm (No. 129) which is nonsymmorphic. The point group of the Bravais lattice is D_{4h} . The nonsymmorphic symmetries within a unit cell include both screw axes and glide planes. We have performed detailed band structure calculations of LaPt₃P using density functional theory (DFT). The corresponding band structure results with and without spin orbit coupling (SOC) are shown in Fig. 5(a) and Fig. 5(b) respectively. We note that this material has significant splitting of bands due to SOC [5]. The maximum band splitting caused by the SOC near the Fermi level is estimated to be ~ 120 meV and is most apparent along the MX high symmetry direction. The SOC induced band splitting breaks the spin-symmetry and have important consequences in Cooper-pairing in this material.

The 3D Fermi surfaces were plotted by the XCrySDen packages [6]. The Fermi surfaces with SOC are shown in Fig. 6. We note that there are four Fermi surfaces with the middle two shown in Fig. 6(b) and Fig. 6(c); and again

in Fig. 6(f) and Fig. 6(g) from a different view, contributing the most to the density of states (DOS) at the Fermi level. This is seen from the projected DOS at the Fermi level shown in Fig. 7. Fig. 7(a) shows the contributions of the different atomic orbitals to the DOS at the Fermi level. We note that Pt-5d orbitals contribute the most. Thus LaPt₃P is a multi-band system. Fig. 7(a) shows the contributions of the different Fermi surfaces to the DOS at the Fermi level.

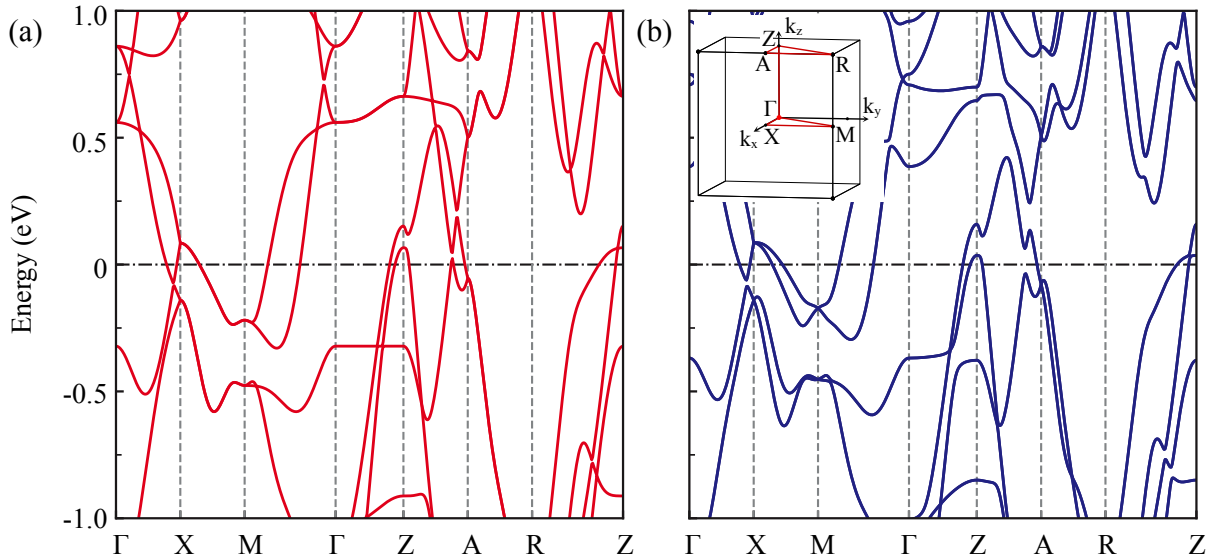


FIG. 5. **First principles band structure results of LaPt₃P.** a) Band structure without SOC. b) Band structure with SOC. The primitive tetragonal Brillouin zone with the marked high symmetry points and directions used in the band structure computation is shown in the inset of (b). We note that SOC induces significant band splitting near the Fermi level especially from M to X.

V. SYMMETRY ANALYSIS

In this section we describe, the symmetry analysis of the possible superconducting order parameters for LaPt₃P. To proceed, we note the properties of the material: it is centrosymmetric, has nonsymmorphic symmetries, has considerable effects of SOC, has multiple bands potentially participating in superconductivity, has spontaneously broken TRS at T_c and has line nodes dominating its thermodynamic behavior.

The normal state symmetry group of the system is given by $\mathcal{G} = G_0 \otimes U(1) \otimes \mathcal{T}$, where $U(1)$ is the gauge symmetry group, G_0 is the group of symmetries containing the point group symmetries of D_{4h} and spin rotation symmetries in 3D of $SO(3)$ and \mathcal{T} is the group of time-reversal symmetry (TRS). The Ginzburg-Landau (GL) free energy of the system must be invariant under this symmetry group.

The D_{4h} point group has 8 one-dimensional irreducible representations (irreps) (4 of them have even parity and the other 4 have odd parity) and 2 two dimensional irreps (one with even parity denoted by E_g and the other with odd parity denoted by E_u). Centrosymmetry implies that this material has either purely triplet or purely singlet superconducting instability in general. Furthermore, a TRS breaking superconducting order parameter requires degenerate or multi-dimensional irreps. This system can thus lead to such type of instability only in the E_g or the E_u irrep. We will now focus only on these two irreps and construct possible superconducting order parameters for the system. We consider strong SOC as uncovered by the band structure calculation of this material.

The fourth order invariant corresponding to the 2 two-dimensional irreps E_g and E_u of D_{4h} gives the quartic order term of the GL free energy [7, 8] to be

$$f_4 = \beta_1(|\eta_1|^2 + |\eta_2|^2)^2 + \beta_2|\eta_1^2 + \eta_2^2|^2 + \beta_3(|\eta_1|^4 + |\eta_2|^4) \quad (5)$$

where (η_1, η_2) are the two complex components of the two-dimensional order parameters. This free energy needs to be minimized with respect to both η_1 and η_2 . The nonequivalent solutions are: $(\eta_1, \eta_2) = (1, 0)$, $\frac{1}{\sqrt{2}}(1, 1)$ and

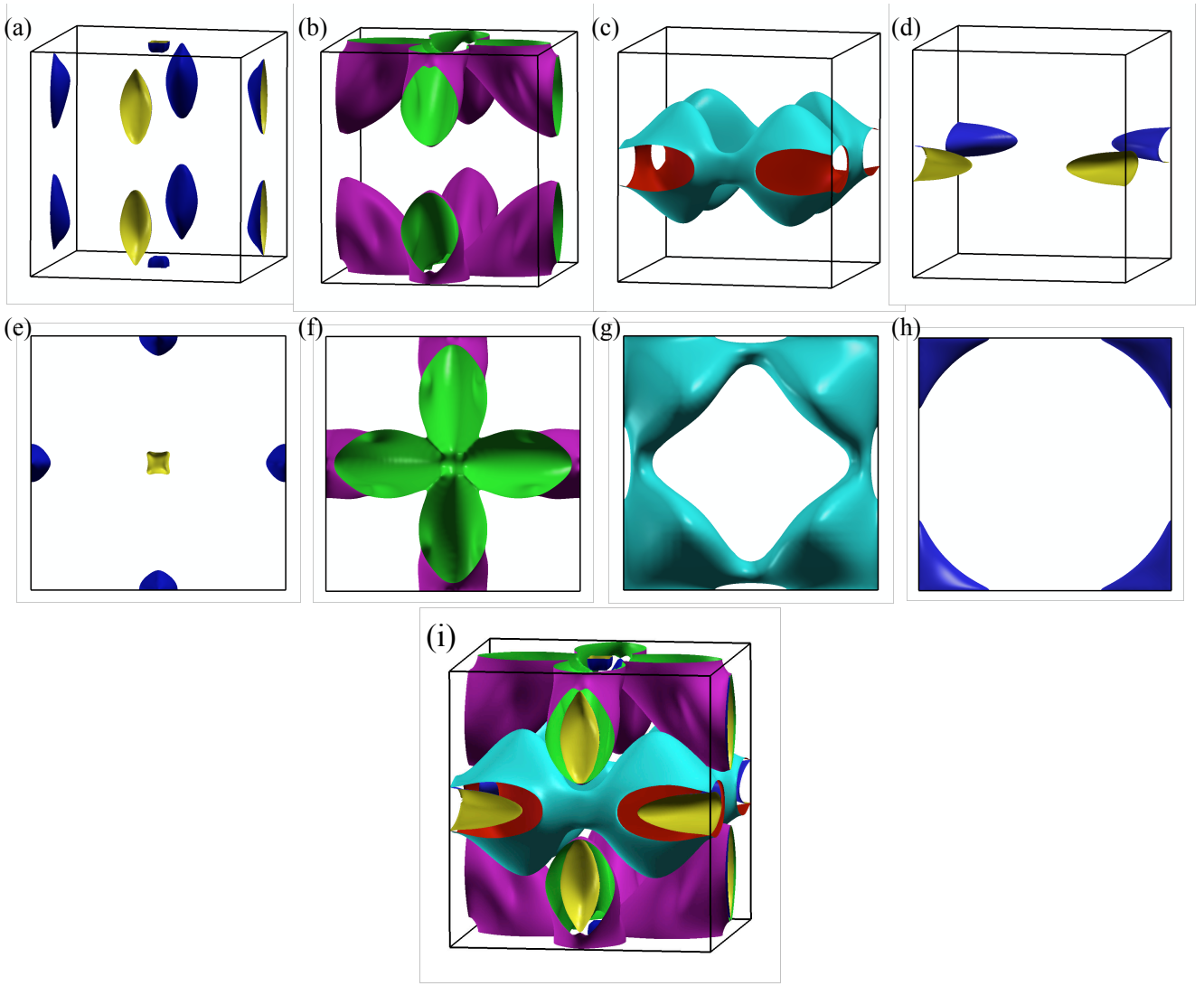


FIG. 6. **Fermi surfaces of LaPt₃P with SOC.** Panels (a)–(d) are from a side view and the panels (e)–(h) are from the top view for the four Fermi surface sheets and (i) shows a combined Fermi surface.

$\frac{1}{\sqrt{2}}(1, i)$. There is an extended region in the parameter space where the states corresponding to $(\eta_1, \eta_2) = (1, i)$ is stabilized. The instabilities corresponding to this case spontaneously break TRS at T_c due to a nontrivial phase difference between the two order parameter components.

Then the even parity superconducting order parameter belonging to E_g is given by

$$\Delta(\mathbf{k}) = \Delta_0 k_z (k_x + i k_y) \quad (6)$$

where Δ_0 is the real amplitude independent of \mathbf{k} . This is a *chiral d-wave* singlet order parameter. The odd parity superconducting order parameter belonging to E_u gives rise to the gap matrix $\hat{\Delta}(\mathbf{k}) = [\mathbf{d}(\mathbf{k}) \cdot \vec{\sigma}] i \sigma_y$ where $\vec{\sigma}$ denotes the three Pauli spin matrices and $\mathbf{d}(\mathbf{k})$ is the triplet *d*-vector given by

$$\mathbf{d}(\mathbf{k}) = [A k_z, i A k_z, B(k_x + i k_y)]. \quad (7)$$

Here, A and B are material dependent real constants independent of \mathbf{k} and in general they are nonzero. We note that the values of A and B determine the orientation of the *d*-vector. For example, for $A = 0$ the *d*-vector points along the *c*-axis and for $B = 0$ the *d*-vector points in the *ab*-plane. We also note that

$$\mathbf{d}(\mathbf{k}) \times \mathbf{d}^*(\mathbf{k}) = 2i A k_z (B k_x \hat{x} - B k_y \hat{y} - A k_z \hat{z}) \quad (8)$$

which is nonzero in general. Hence, this superconducting state is *nonunitary chiral p-wave* triplet state.

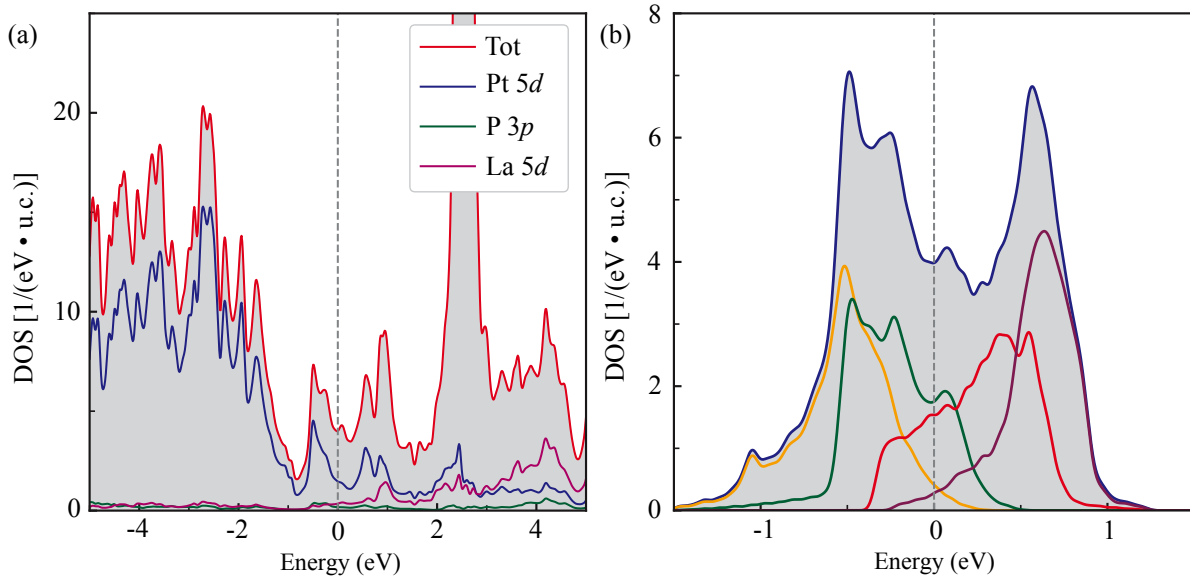


FIG. 7. **Projected density of states (DOS) results.** Left panel shows the contributions of different orbitals to the DOS. We note that Pt 5d orbitals contribute the most to the DOS at the Fermi level. The right panel shows the DOS contributions of the different Fermi surfaces. The blue is total and the other four correspond to the four Fermi surfaces. Their contributions at the Fermi level are 10.3%, 43.4%, 39.5% and 6.3%.

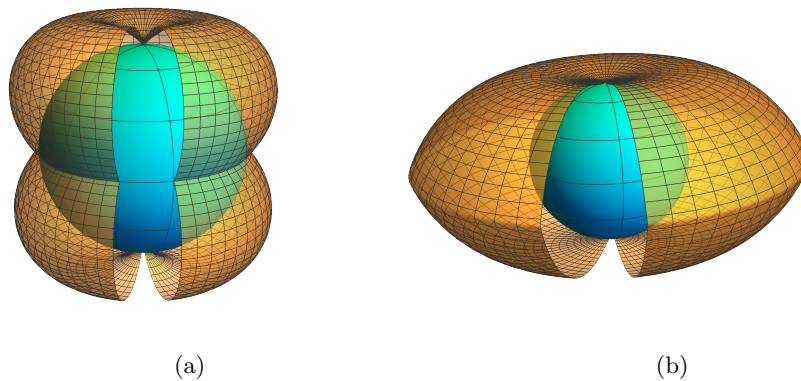


FIG. 8. **Polar plots of the excitation energy gaps.** (a) The chiral d -wave singlet case and (b) the nonunitary chiral p -wave triplet case. In both the cases, point nodes appear at the two “poles”, while the singlet case has an additional line node at the “equator”.

The strong SOC case considered here implies that the single particle states are no longer the eigenstates of spin and we need to label them rather by pseudospins. The pseudospin states are linear combinations of the spin eigenstates. Since the pseudospin and the spin are closely related, the even parity states correspond to pseudospin singlet and the odd parity states correspond to pseudospin triplet states.

We can now follow the standard Bogoliubov-de Gennes mean field theory [8] to compute the quasi-particle excitation energy spectrum for the two TRS breaking states given in Eqn. (6) and Eqn. (7). The schematic view of the excitation energy gaps for the two order parameters are shown in Fig. 8.

VI. TOPOLOGICAL PROPERTIES OF THE CHIRAL SINGLET STATE

To discuss the topological properties of the nodal excitations for the chiral d -wave state with the gap function

$$\Delta(\mathbf{k}) = \frac{\Delta_0}{k_F^2} k_z (k_x + ik_y) \quad (9)$$

with Δ_0 being the pairing amplitude, we assume a simplified single band parabolic dispersion (in units of \hbar)

$$\xi(\mathbf{k}) = \frac{k^2}{2m} - \mu, \quad (10)$$

where m is the mass of an electron, $\mu = \frac{k_F^2}{2m}$ is the chemical potential and k_F is the Fermi wavevector. We note that $\Delta(\mathbf{k}) \sim Y_1^2(\theta, \phi)$ where $Y_m^l(\theta, \phi)$ are the spherical harmonics. Thus the Cooper pairs have an angular momentum $L_z = +1$ for this state.

Then Bogoliubov-de Gennes Hamiltonian in the pseudospin basis can be written as

$$\mathcal{H} = \sum_{\mathbf{k}} \Psi_{\mathbf{k}}^\dagger H(\mathbf{k}) \Psi_{\mathbf{k}} \quad (11)$$

where $\Psi_{\mathbf{k}} = (c_{\mathbf{k}\uparrow}, c_{-\mathbf{k}\uparrow}^\dagger)^T$ with $c_{\mathbf{k}\sigma}$ being the fermion annihilation operator with pseudospin flavor $\sigma \in \{\uparrow, \downarrow\}$. We can rewrite the BdG Hamiltonian as

$$H(\mathbf{k}) = \mathbf{N}(\mathbf{k}) \cdot \boldsymbol{\tau} \quad (12)$$

where $\boldsymbol{\tau}$ is the vector of the three Pauli matrices in the particle-hole space and $\mathbf{N}(\mathbf{k}) = \left\{ \frac{\Delta_0}{k_F^2} k_z k_x, \frac{\Delta_0}{k_F^2} k_z k_y, \xi(\mathbf{k}) \right\}$ is a pseudospin vector. The eigenvalues of the Hamiltonian in Eqn. (12) are $\pm E(\mathbf{k})$ where

$$E(\mathbf{k}) = |\mathbf{N}(\mathbf{k})| = \sqrt{\xi^2(\mathbf{k}) + |\Delta(\mathbf{k})|^2}. \quad (13)$$

Hence, the superconducting ground state has two point nodes at the two poles of the Fermi surface $\mathbf{k}_\pm = (0, 0, \pm k_F)$ and a line node at the equator $k_z = 0$ plane. The low energy Hamiltonian close to two point nodes can be written as

$$H(\mathbf{k}) = \frac{\Delta_0}{k_F} (p_x \tau_x - p_y \tau_y) \pm v_F p_z \tau_z \quad (14)$$

where we have defined $\mathbf{p} = (\mathbf{k} - \mathbf{k}_\pm)$. This is a Weyl Hamiltonian. Thus the two point nodes are also Weyl nodes. As a result they are impossible to gap out since there is no fourth Pauli matrix which can come from a mass term to gap out the nodes.

The corresponding Bloch wave functions $|u_\pm(\mathbf{k})\rangle$ are the eigenfunctions of $\hat{\mathbf{n}}(\mathbf{k}) \cdot \boldsymbol{\sigma}$ with eigenvalues ± 1 where $\hat{\mathbf{n}}(\mathbf{k}) = \mathbf{N}(\mathbf{k})/|\mathbf{N}(\mathbf{k})|$ is the unit vector along the direction of the pseudospin $\mathbf{N}(\mathbf{k})$. We note that this unit vector $\hat{\mathbf{n}}(\mathbf{k})$ is well defined only when $|\mathbf{N}(\mathbf{k})| \neq 0$ i.e. in the nodeless regions on the Fermi surface. In spherical coordinates, parametrizing $\hat{\mathbf{n}}(\mathbf{k}) = [n_x(\mathbf{k}), n_y(\mathbf{k}), n_z(\mathbf{k})] = [\sin(\theta) \cos(\phi), \sin(\theta) \sin(\phi), \cos(\theta)]$ we have

$$|u_-(\mathbf{k})\rangle = \begin{bmatrix} \cos(\frac{\theta}{2}) e^{-i\phi} \\ \sin(\frac{\theta}{2}) \end{bmatrix} \quad \text{and} \quad |u_+(\mathbf{k})\rangle = \begin{bmatrix} \sin(\frac{\theta}{2}) e^{-i\phi} \\ -\cos(\frac{\theta}{2}) \end{bmatrix}. \quad (15)$$

Then from the negative energy occupied states $|u_-(\mathbf{k})\rangle$ the Berry connection is defined as

$$\mathbf{A}(\mathbf{k}) = i \langle u_-(\mathbf{k}) | \nabla_{\mathbf{k}} | u_-(\mathbf{k}) \rangle \quad (16)$$

and the corresponding Berry curvature is $\mathbf{F}(\mathbf{k}) = \nabla_{\mathbf{k}} \times \mathbf{A}(\mathbf{k})$. In terms of the components of $\hat{\mathbf{n}}(\mathbf{k})$, it is given by $\mathbf{F}(\mathbf{k}) = [n_y(\mathbf{k}) \{ \nabla_{\mathbf{k}} n_z(\mathbf{k}) \times \nabla_{\mathbf{k}} n_x(\mathbf{k}) \} - n_x(\mathbf{k}) \{ \nabla_{\mathbf{k}} n_z(\mathbf{k}) \times \nabla_{\mathbf{k}} n_y(\mathbf{k}) \}] / [2 \{ n_x^2(\mathbf{k}) + n_y^2(\mathbf{k}) \}]$.

For the chiral d -wave case, $F_x(\mathbf{k})$ and $F_y(\mathbf{k})$ are odd functions of (k_y, k_z) and (k_x, k_z) respectively. Hence, there is no Berry flux along the x and y directions. The number of field lines coming in and out of the ca and cb planes are the same. Whereas $F_z(\mathbf{k})$ is an even function of (k_x, k_y) and the flux through the ab plane as a function of k_z is

$$\Phi(\mathbf{k}) = \int dk_x dk_y F_z(\mathbf{k}) = 2\pi \mathcal{C}(k_z). \quad (17)$$

$\mathcal{C}(k_z)$ is the "sliced" Chern number (momentum dependent) of the effective 2D problem for a fixed k_z . For a given value of $|k_z| < k_F$, the Hamiltonian in Eqn. (12) describes an effective 2D problem with fully gapped weak coupling BCS pairing and an effective chemical potential $\frac{\hbar^2}{2m}(k_F^2 - k_z^2)$ having the Chern number $\mathcal{C}(k_z) = +1$. For $|k_z| > k_F$, the effective chemical potential is negative and describes a topologically trivial BEC state. Thus, the Weyl point nodes at $(0, 0, \pm k_F)$ act as monopoles and anti-monopoles of the Berry curvature and the flux through a sphere surrounding the monopole is 2π and that through the anti-monopole is -2π . The topologically protected Weyl nodes give rise to Majorana arc surface states on the surface Brillouin zone corresponding to the $(1, 0, 0)$ and $(0, 1, 0)$ surfaces having

chiral linear dispersions along y and x directions respectively. As a result of the arc surface states the system shows anomalous thermal and spin Hall effects [9–11].

The equatorial line node is characterized by a 1D winding number. This can be defined in terms of the following spectral symmetry [10, 11] of the Hamiltonian. We note that the operator

$$\Gamma_{\mathbf{k}} = \sin(\phi_{\mathbf{k}})\tau_x + \cos(\phi_{\mathbf{k}})\tau_y \quad (18)$$

where $\tan(\phi_{\mathbf{k}}) = k_y/k_x$ anticommutes with the Hamiltonian

$$\{H(\mathbf{k}), \Gamma_{\mathbf{k}}\} = 0. \quad (19)$$

As a result any eigenstate of the Hamiltonian $H(\mathbf{k})$ with the eigenvalue $E_{\mathbf{k}}$ is also an eigenstate of the operator $\Gamma_{\mathbf{k}}$ with the eigenvalue $-E_{\mathbf{k}}$. Then with the help of this spectral symmetry $\Gamma_{\mathbf{k}}$ we define the winding number as

$$w(\mathbf{k}_{\perp}) = -\frac{1}{4\pi i} \oint_{\mathcal{L}} dl \text{Tr} [\Gamma_{\mathbf{k}} H^{-1}(\mathbf{k}) \partial_l H(\mathbf{k})], \quad (20)$$

where dl is the line element along a closed loop \mathcal{L} encircling the line node and $\mathbf{k}_{\perp} = (k_x, k_y)$. For this case then we have

$$w(\mathbf{k}_{\perp}) = 1 \quad \forall k_{\perp} < k_F \quad (21)$$

$$= 0 \quad \text{otherwise.} \quad (22)$$

We note that the winding number does not depend on the angular momentum of the Cooper pairs. This nontrivial topology of the line node ensures the existence of zero-energy surface Andreev bound states on the $(0, 0, 1)$ surface. They produce an image of the Fermi surface equator in the corresponding surface Brillouin zone. Being dispersionless, these zero-energy states result in a divergent density of states, and are predicted to give rise to a zero bias peak in tunneling measurements. These zero modes are two fold degenerate Majorana fermions arising from the twofold spin degeneracy of the pairing interaction.

* pabitra.biswas@stfc.ac.uk

† S.Ghosh@kent.ac.uk

- [1] T. Takayama, K. Kuwano, D. Hirai, Y. Katsura, A. Yamamoto, and H. Takagi, “Strong Coupling Superconductivity at 8.4 K in an Antiperovskite Phosphide SrPt₃P,” *Phys. Rev. Lett.* **108**, 237001 (2012).
- [2] A. A. Coelho, “*TOPAS* and *TOPAS-Academic*: an optimization program integrating computer algebra and crystallographic objects written in C++,” *Journal of Applied Crystallography* **51**, 210–218 (2018).
- [3] N. D. Zhigadlo, “High pressure crystal growth of the antiperovskite centrosymmetric superconductor SrPt₃P,” *Journal of Crystal Growth* **455**, 94 – 98 (2016).
- [4] A. Yaouanc and P. Dalmas de Réotier, *Muon Spin Rotation, Relaxation, and Resonance: Applications to Condensed Matter* (Oxford University Press, Oxford, 2011).
- [5] H. Chen, X. Xu, C. Cao, and J. Dai, “First-principles calculations of the electronic and phonon properties of APt₃P ($A = \text{Ca, Sr, and La}$): Evidence for a charge-density-wave instability and a soft phonon,” *Phys. Rev. B* **86**, 125116 (2012).
- [6] A. Kokalj, “Computer graphics and graphical user interfaces as tools in simulations of matter at the atomic scale,” *Computational Materials Science* **28**, 155–168 (2003).
- [7] J. F. Annett, “Symmetry of the order parameter for high-temperature superconductivity,” *Adv. Phys.* **39**, 83–126 (1990).
- [8] M. Sigrist and K. Ueda, “Phenomenological theory of unconventional superconductivity,” *Rev. Mod. Phys.* **63**, 239–311 (1991).
- [9] A. P. Schnyder and P. M. R. Brydon, “Topological surface states in nodal superconductors,” *Journal of Physics: Condensed Matter* **27**, 243201 (2015).
- [10] P. Goswami and A. H. Nevidomskyy, “Topological Weyl superconductor to diffusive thermal Hall metal crossover in the B -phase of UPt₃,” *Phys. Rev. B* **92**, 214504 (2015).
- [11] P. Goswami and L. Balicas, “Topological properties of possible Weyl superconducting states of URu₂Si₂,” arXiv preprint arXiv:1312.3632 (2013).